Journal of Colloid and Interface Science 630 (2023) 249–259

Contents lists available at ScienceDirect

Journal of Colloid and Interface Science

journal homepage: www.elsevier.com/locate/jcis

Self-assembly of cellulose nanocrystals of different lengths

Vikram Singh Raghuwanshi *, Christine Browne, Warren Batchelor, Gil Garnier *

Bioresource Processing Research Institute of Australia (BioPRIA), Department of Chemical and Biological Engineering, Monash University, Clayton, Victoria 3800, Australia

GRAPHICAL ABSTRACT

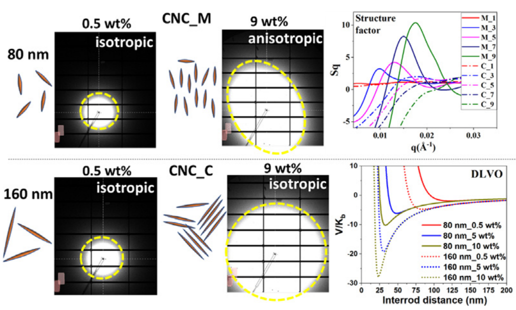

ARTICLE INFO

Article history:
Received 15 August 2022
Revised 17 October 2022
Accepted 19 October 2022
Available online 25 October 2022

Keywords:
Self-assembly
Cellulose Nanocrystals (CNC)
Small Angle X-ray Scattering (SAXS)
DLVO
Transmission Electron Microscopy (TEM)
Polarised Optical Microscopy (POM)

ABSTRACT

Hypothesis

The self-assembly (SA) of cellulose nanocrystals (CNC) in suspensions is important both from the fundamental and advanced technology development perspective. CNC of different lengths self-assemble differently in suspensions by balancing attractive and repulsive interactions which depends strongly on morphology, surface chemistry and concentrations.

Experiments

Two different commercial CNC samples (CNC-**M** and CNC-**C**) of different lengths were dispersed in Milli-Q water at different concentrations (0.5–10 wt%). CNC-**M** is provided as a gel at a solid concentration of 10.3 wt% which was diluted in Milli-Q water. CNC-**C** is sold as a powder which was dispersed in Milli-Q water with a mixer to achieve the desired concentrations. TEM was used to determine morphology of CNC. Polarised optical microscopy is performed to get microscale visualisation of the chiral nematic self-assembly. High flux synchrotron SAXS is applied to evaluate and compare the nanoscale self-assembly mechanisms of CNC of different lengths.

Findings

The SA of two different types of CNC rods of similar diameter but different lengths is investigated. SAXS analysis shows the short rods in suspension form an isotropic phase (randomly oriented) at lower concentration (0–4 wt%); as concentration is increased, the rods become systematically aligned in a nematic phase. The interrod distance d varies as $c^{-0.33}$ at the lower concentration, which changes to $c^{-0.5}$ and even c^{-1} at the higher concentrations. In contrast, the long rods in suspension remain in the isotropic phase throughout the measured concentration range from 0.5 to 10 wt%. The interrod distance also follows the isotropic power law slope of $c^{-0.33}$. Suspensions made of the short CNC rods show long range order and large interrod distance compared to those formed by the long rods. POM agrees with the SAXS

* Corresponding authors.
E-mail addresses: vikram.raghuwanshi@monash.edu (V.S. Raghuwanshi), gil.garnier@monash.edu (G. Garnier).

https://doi.org/10.1016/j.jcis.2022.10.100
0021-9797/

results. A specific equilibrium between attractive and repulsive forces is required to maintain SA and ordering of the rods. DLVO calculations reveal that the long rods maintain van der Waal attractive force dominating over the electrostatic repulsion, which hinders rods alignment in an ordered manner. However, for the short rods, the weaker attractive interactions are well compensated by the repulsive force which aligns rods in an ordered assembly. This fundamental understanding of the SA of rods in suspensions facilitates the engineering of novel CNC composites of unique optical properties which enables novel applications such as in sensors and bio-diagnostics.

1. Introduction

Cellulose nanocrystals (CNC) are a sustainable polymer which has shown great potential in replacing non-biodegradable materials in advanced technologies [1,2]. CNC exhibits properties of low density, high strength, high crystallinity, liquid crystalline (LC) behaviour, recyclability and biodegradability properties which have created a demand which is significantly increasing every year [3]. With this gain in popularity, CNC are interesting both for their fundamental behaviour and to engineer advanced and functional materials [4–6]. The fundamentals of CNC rods self-assembly (SA) allow to modulate the LC behaviour from isotropic to cholesteric, and nematic phases [4,7,8]. In the isotropic phase, the rods are randomly oriented; in the nematic phase, the rods are aligned in a particular direction. While in the chiral nematic phase, the CNC rods are aligned in the direction of director **n**, which is helically organised along the perpendicular axis to **n** [9,10]. Use of external magnetic field, electric field and shear further allow aligning the rods from a chiral nematic to a nematic transition [11–13]. Similar SA behaviour was well-studied for the rods from tobacco mosaic virus (TMV) and fd virus in suspension [14]. The controlled ordering of CNC in different liquid crystalline phases is used to manufacture advanced optics, electronics, energy, sensors devices as well as bio-diagnostics [15,16].

The SA of CNC in different phases is monitored by calculating interrod distance, twist angle between rods, pitch size, translational and rotational dynamics, and performing a force balance (attractive and repulsive) of the suspension system [17,18]. These SA parameters depend upon the morphology and surface chemistry of CNC, their concentration, the ionic strength and pH of the suspension [19,20]. Onsager reveals the formation of different LC phases is due to competition between the translation and the rotation entropy at different concentrations [21]. At lower concentrations, the dominating rotational entropy leads to move particles in all directions into random orientations. While above a threshold concentration, the translation entropy (movement in a particular direction) domination leads to phase separation as the rods align in a particular direction [22]. Furthermore, the large aspect ratio of CNC leads to a lower percolation threshold concentration compared to the smaller aspect ratio CNC rods [3,23]. The high ionic strength of the suspension brings the rods closer [24].

The balance between van der Waals attraction and electrostatic repulsion also plays a crucial part in the formation of LC phases. During SA, the attractive forces bring the rods closer to each other and in a parallel alignment; the repulsive forces promote orthogonal ordering [25,26]. The Derjaguin, Landau, Verwey, and Overbeek (DLVO) theory is well established to determine the resultant potential originating from the van der Waals and electrical double layer repulsion [27,28]. A proper balance between these forces is important to tailor the SA in the LC phases of the system. An imbalance can lead to the aggregation or random distribution of the rods in the suspension. Thus, clear understanding on the effect of excessive attraction or repulsion between the nanocellulose rods is needed to engineer their assembly in liquid crystal phase in suspension.

Commercial CNC made from different companies can have different morphology (length, diameter, distribution) and surface chemistry [3,29], even when using the same raw material. Variations in these parameters affect the strength and range of attractive and repulsive forces, and thus the self-assembly of rods in suspension. It is important to understand the self-assembly of commercial CNC rods in their received forms. Further, proper benchmarking is required to analyse the concentration dependent LC phase transitions. This helps in manipulating their optical properties for specific purposes, by choosing the type of treatment used for tailoring their phase separations.

In this study, we quantify the self-assembly of the two dominant commercial cellulose nanocrystals in aqueous suspension. The two different CNC were both made by sulfuric acid hydrolysis using a softwood pulp. They have similar surface chemistry (zeta potential and sulfur groups) and diameters but different lengths. The CNC were diluted in MilliQ water to achieve suspensions ranging in concentration from 0.5 to 10 wt%. The objective is to better understand how the length affects the CNC self-assembly at different concentrations. DLVO calculation guides the prediction of the SA mechanism of suspensions of these CNC differing in lengths by balancing attractive and repulsive interactions. We aim at quantifying how the CNC self-assembly mechanism depends on morphology and concentrations. Transmission electron microscopy (TEM) is used to visualise and determine shape and size of CNC. Small angle X-ray scattering (SAXS) was selected to quantify the self-assembly, morphology and interrod distance as a function of CNC concentration. This study aims at providing the engineering fundamentals to modulate optical and electric properties of CNC-based material for sensor, bio-diagnostics and energy applications.

2. Experimental

2.1. Materials

Two different commercial CNC samples were purchased from the Process Development Center in University of Maine, USA (CNC-**M**) and CelluForce, Pointe Claire, Canada (CNC-**C**). CNC-**M** is sold as a gel at a solid concentration of 10.3 wt%. The samples of the different concentrations were diluted in Milli-Q water. The CNC-**C** is received as a powder obtained by spray drying. The powder was dispersed in Milli-Q water by a dispersant mixer to achieve the desired concentrations. Both CNC samples were studied at concentrations ranging between 0.5 and 10 wt%. The zeta potential, sulfur content and sulfate half-ester content were measured on the similar set of samples in the recent publication [30]. The zeta potential of the CNC-**M** and CNC-**C** was −50 ± 6 mV and −54 ± 6 mV, respectively. The elemental sulphur content (%S) of CNC-**M** was 0.73 ± 0.09 and 0.57 ± 0.06 for CNC-**C**. The sulphate half-ester content (mmol/g) for CNC-**M** and CNC-**C** were 0.23 ± 0.03 and 0.18 ± 0.02.

2.2. Transmission electron microscopy (TEM)

Transmission electron microscopy analysis was performed at the Ian Holmes Imaging Centre of University of Melbourne, Australia. The diluted CNC suspension of 0.01 wt% concentration was dropped on the quantifoil and copper grids and dried at ambient conditions. The TEM imaging was performed on the FEI Tecnai F20 TEM instrument in the STEM mode using HAADF detector. ImageJ software is used for TEM image analysis.

2.3. Polarised optical microscopy (POM)

Polarised optical microscopy was performed on the Nikon Eclipse Ni-U microscope equipped with two crossed linear polarisers. Different concentrations of CNC-**C** and CNC-**M** were made in the MilliQ water. The diluted CNC suspensions were placed into flat glass capillaries (inner dimensions: 0.5 mm $\times$ 5 mm). The samples were measured in the transmission mode at room temperature.

2.4. Small angle X-ray scattering (SAXS)

Small angle X-ray scattering experiments were made at the high flux SAXS/WAXS beamline of the Australian Synchrotron [31]. The samples were prepared fresh and filled in the quartz capillaries (1.5 mm thick). The quartz capillaries were measured vertically in the transmission mode. The X-ray exposure time was 3 s per sample. All samples were measured two days after placing in the capillaries. The X-ray energy is 12 KeV. The Pilatus detector was used to collect the scattered X-rays. Silver behenate and glassy carbon are used to calibrate the q values and intensity in the absolute value of cross section. The samples were measured at the large sample to detector distance of 7 m which covers a large size range. The data reduction was performed by the inhouse software ScatterBrain. The SAXS curves were fitted with the open source SASfit software [38].

3. Results

The morphology and size distribution of both CNC samples were characterized by high-resolution transmission electron microscopy (TEM). Fig. 1a shows the TEM micrograph of the CNC-**M** sample and Fig. 1b that of the CNC-**C**. The image analysis shows both types of CNC are rod shaped with a similar diameter of 4–6 nm. Detailed analysis on determining the length of CNC rods are reported in our recent publication [30]. The measured length of CNC-**M** is 88.9 ± 37.5 nm, while CNC-**C** is twice as long with an average length of 141.5 ± 60 nm. TEM provides the local area information; however, the aggregation of the CNC during sample preparation can lead to misleading information. It is also difficult to assess self-assembly (SA) from electron micrographs. To reveal the structure and SA arrangement information from the CNC aqueous suspension polarised optical microscopy (POM) and small angle X-ray scattering (SAXS) were performed.

Polarised optical microscopy (POM) is made on the CNC-**C** and CNC-**M** at different concentrations from 3 wt% to 7 wt% (Fig. 2). CNC suspension of lower concentrations (<2 wt%) does not show any self-assembly. The CNC-**C** 3 wt% shows randomly distributed tactoid structures (Fig. 2a). Higher concentrations of CNC-**C** (5 wt % and 7 wt%) show similar tactoid formation and random distributions. However, CNC-**M** 3 wt% shows small chiral nematic structure domains which are distributed randomly (Fig. 2b). Increasing CNC-**M** concentration to 5 wt% increases the self-assembly (domains) of the rods with decrease in the pitch size. Further increase of CNC-**M** concentration to 7 wt% enhances rod self-assembly in a long-range order with further decrease in the pitch size. The inset shows an enlarged image of the region showing long range assembly of CNC-**M** rods. Higher concentration (>7 wt%) of both CNC samples are too viscous to fill in the capillary and difficult to image. POM provides information at the microscale and allows direct visualisation of the chiral nematic assembly. However, by POM it is difficult to get information on the nanoscale interrod distance and access information at a complete range of concentrations from 0.5 wt% to 10 wt%. Thus, small angle X-ray scattering (SAXS) is performed to reveal CNC self-assembly information in the size range from 1 to 100 nm [32–34].

The distribution of the scattered X-rays from the suspension on the detector shows the SA of CNC rods in suspension. The isotropic scattering reveals the random distribution of rods, while the anisotropic distribution discloses that the rods are aligned in a particular direction. The CNC-**M** sample for 0.5 wt% is isotropic, which becomes partly anisotropic at 5 wt% and develops as anisotropic at a concentration of 9 wt% (Fig. 3a). Azimuthal averaging of scattering images shows clarity in the isotropic and anisotropic scattering (supporting information S1). However, the CNC-**C** shows the isotropic scattering for the full concentration range from 0.5 wt% to 9 wt% (Fig. 3b). The scattering intensity increases with increasing concentrations, indicating a higher number of CNC rods in the suspensions.

The SAXS images were radially averaged into the scattering curves which is a plot of scattering intensity as a function of scattering vector q (Fig. 4a). The magnitude of scattering vector is

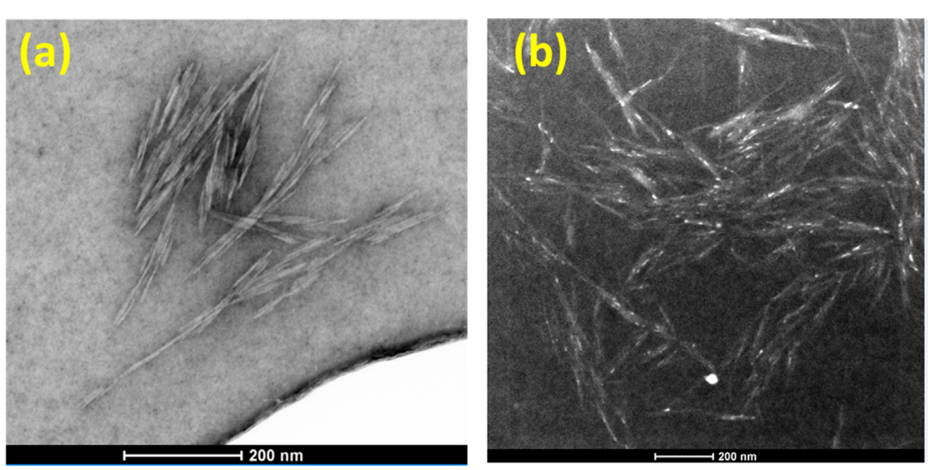

Fig. 1. Transmission electron micrograph (TEM) of two different commercial cellulose (a) CNC-**M** (on quantifoil grid) (b) CNC-**C** (on copper grid).

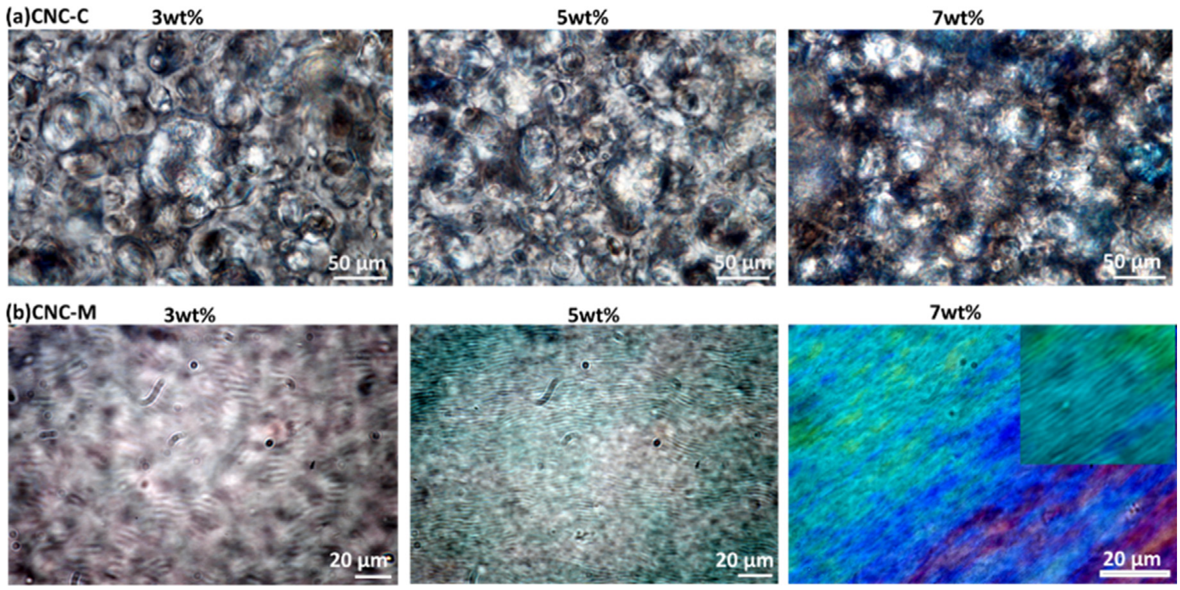

Fig. 2. Polarised optical microscopy (POM) images of two different commercial cellulose (a) CNC-**C** suspension of 3 wt%, 5 wt% and 7 wt% (b) CNC-**M** suspension of 3 wt%, 5 wt % and 7 wt%. The inset in the 7 wt% shows the magnification of the chiral nematic arrangement.

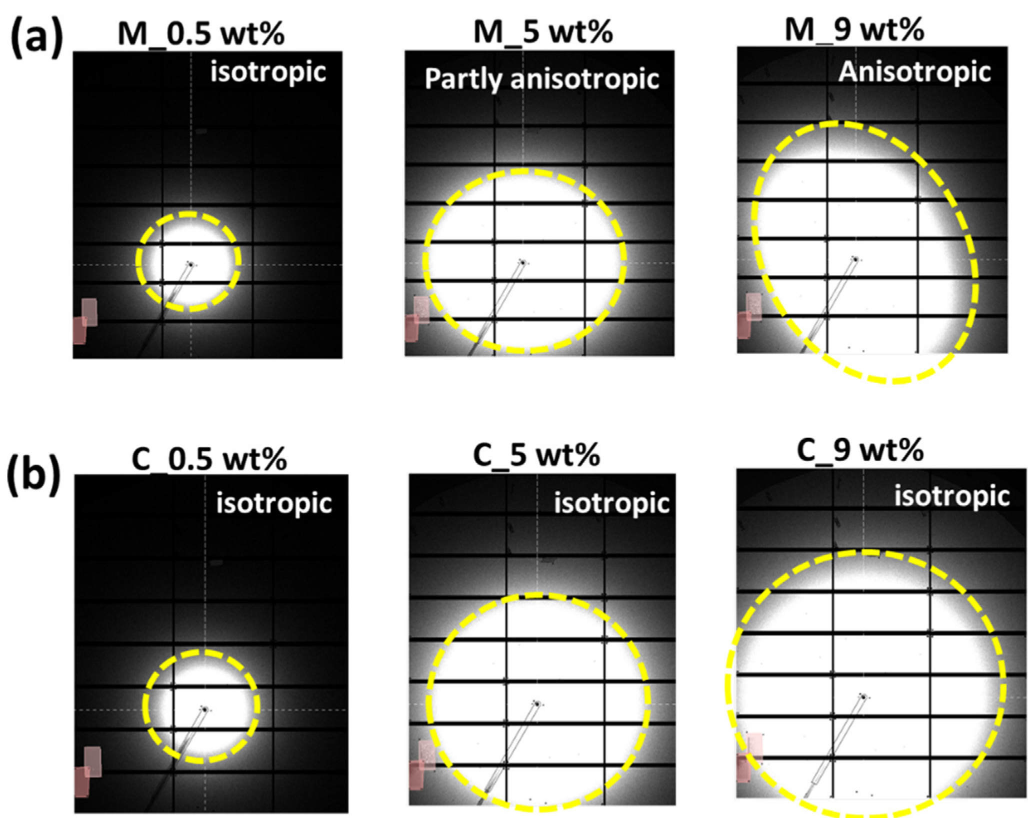

Fig. 3. (a) SAXS scattering images of CNC-**M** for low (0.5 wt%), intermediate (5 wt%) and high concentration (9 wt%). (b) CNC-**C** for three different concentrations of 0.5 wt%, 5 wt% and 9 wt%.

related to the X-rays wavelength (λ)and the scattering angle (2θ) as:

$$q = \frac{4\pi\sin\theta}{\lambda} \tag{1}$$

These scattering curves allow quantification of the CNC shape, size and interrod distance and interaction. Fig. 4 shows the SAXS curves for CNC-**M** of different concentrations ranging from 0.5 wt % to 10 wt%. At the lower concentration of 0.5 wt%, no correlation peak was observed, indicating the rods are not interacting and are randomly distributed. Increasing concentration to 1 wt% shows a weak correlation peak at q = 0.001 Å^{-1} which increases in magni-

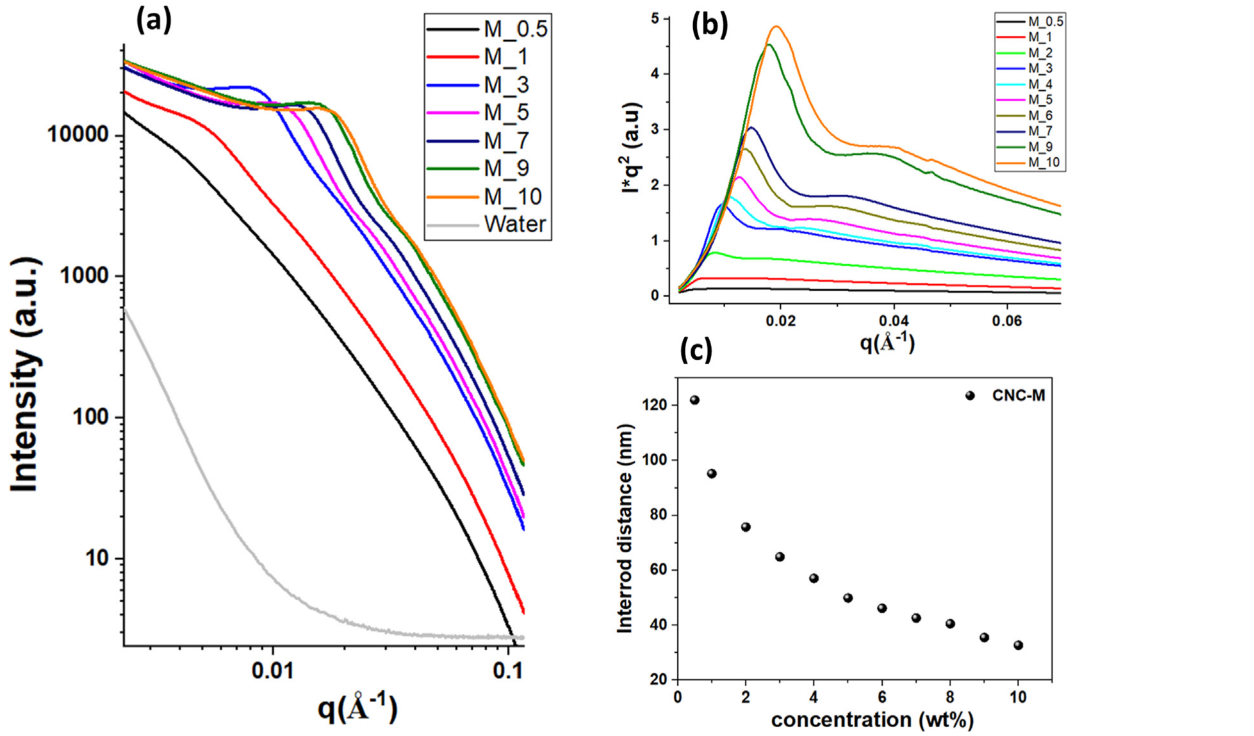

Fig. 4. (a) SAXS scattering curves of CNC-**M** of different concentrations ranging from 0.5 to 10 wt%. The grey curve is for the background from water. (b) The Kratky plot ($I \times q^2$ vs q) of the SAXS curves given in (a). (c) The interparticle distance is plotted as a function of CNC-**M** concentration. The interparticle distance is extracted from the first peak position in the Kratky plot.

tude and shifts towards higher q value with increasing CNC-**M** concentration. The correlation peak is clearly visualised in the Kratky plot (Fig. 4b). The second order peak at q (0.02 $Å^{-1}$) is also pictured at CNC-**M** concentration>3 wt%. The correlation peak position corresponds to the interrod distance 'd' which is determined by the relation $d = 2\pi/q^*$, where q^* is the peak position. The correlation peaks for CNC-**M** are fitted with Lorentz shape peak function to get the centre peak position (q^*). The Lorentz peak function is given by:

$$y = y_0 + \frac{2A}{\pi}\frac{w}{4(x-x_c)^2 + w^2} \quad (2)$$

where y_0 is the offset, x_c is the peak centre, A is the area and w is the full width at half maximum (FWHM). The calculated interrod distance is plotted as a function of CNC concentration (Fig. 4c). There is a large interrod distance of 120 nm observed for the 1 wt% suspension. This interrod distance decreases with increasing CNC-**M** concentration. The result indicates the CNC rods come close to each other at higher concentrations. At the highest concentration of 10 wt%, the interrod distance decreases to 25 nm. The slope of the curves at the higher q value follows the $q^{-\alpha}$ with a $\alpha = 4$ power law, indicating scattering from the surface of the CNC rods. As we move towards lower q value, q varies with $\alpha = 2$, which is an indicator of flat CNC shape and organisation of CNC in a 2D self-assembly, as reported previously [35]. However, the lower q values $q < 0.01$ $Å^{-1}$ follows the value of the $\alpha < 1$ with the dip indicating strong interrod interaction and ordering of rods.

Similarly, the radially averaged SAXS curve for CNC-**C** is shown in Fig. 5a. There is clearly a difference between the SAXS curve profile of CNC-**C** and CNC-**M**. Weak correlation peaks are observed up to 1 wt%. The 2 wt% CNC-**C** shows a correlation peak at q = 0.02 $Å^{-1}$, revealing an average interparticle distance of 50 nm. As the CNC-**C** concentration increases, the correlation peak shifts towards higher q values. This shift of peak towards higher q value reveals a decrease in the interrod distance. Clarity in the peak position is seen in the Kratky plot (Fig. 5b). The interparticle distance as a function of CNC-**C** concentration is shown in Fig. 5c. Interestingly, there is no second order peak observed in the CNC-**C** as detected in the CNC-**M**. This result indicates that the CNC rods are poorly ordered in the long-range scale as compared to CNC-**M**. The power law slope at the lower q value $q < 0.01$ $Å^{-1}$ has the exponent value of $\alpha > 1$ without dips, indicating poor inter-rod interaction and formation of fractals.

The variation of the power law of interrod distance indicates the arrangement of the CNC rods (Fig. 6). In the CNC-**M**, there are three slopes observed; at the lower concentration from 0.5 wt% to 4 wt%, the slope varies with $c^{-0.33}$ which is an indication of the isotropic distribution of the CNC rods. At concentrations between 4 and 8 wt%, the slope varies according to $c^{-0.5}$ which shows the presence of both isotropic and anisotropic arrangement of CNC. The slope for the large wt% between 8 and 10 wt% varies as c^{-1}, revealing the anisotropic distribution of the CNC rods. For CNC-**C** suspensions in the complete measurement range, the slope varies as $c^{-0.33}$, indicating the CNC rods are distributed isotopically in the entire range.

The SAXS curves were then fitted with a shape model (form factor) to determine the shape, size and self-interaction of the nanorod. A rectangular parallelepiped form factor combined with a log normal distribution fits well the scattering curves of 0.5 wt % for both CNC-**C** and CNC-**M** [34,35]. The scattering intensity is a function contains the form factor which is defined as:

$$I(q,a,b,c,\Delta\eta) = \int_0^{\pi}\int_0^{\pi/2}\frac{2}{\pi}\begin{bmatrix} sinc\left(\frac{qa}{2}\sin(\alpha)\cos(\varphi)\right) \\ sinc\left(\frac{qb}{2}\sin(\alpha)\sin(\varphi)\right) \\ sinc\left(\frac{qc}{2}\cos(\varphi)\right)abc\Delta\eta \end{bmatrix}^2 \sin(\alpha)d\alpha d\varphi + Background \quad (3)$$

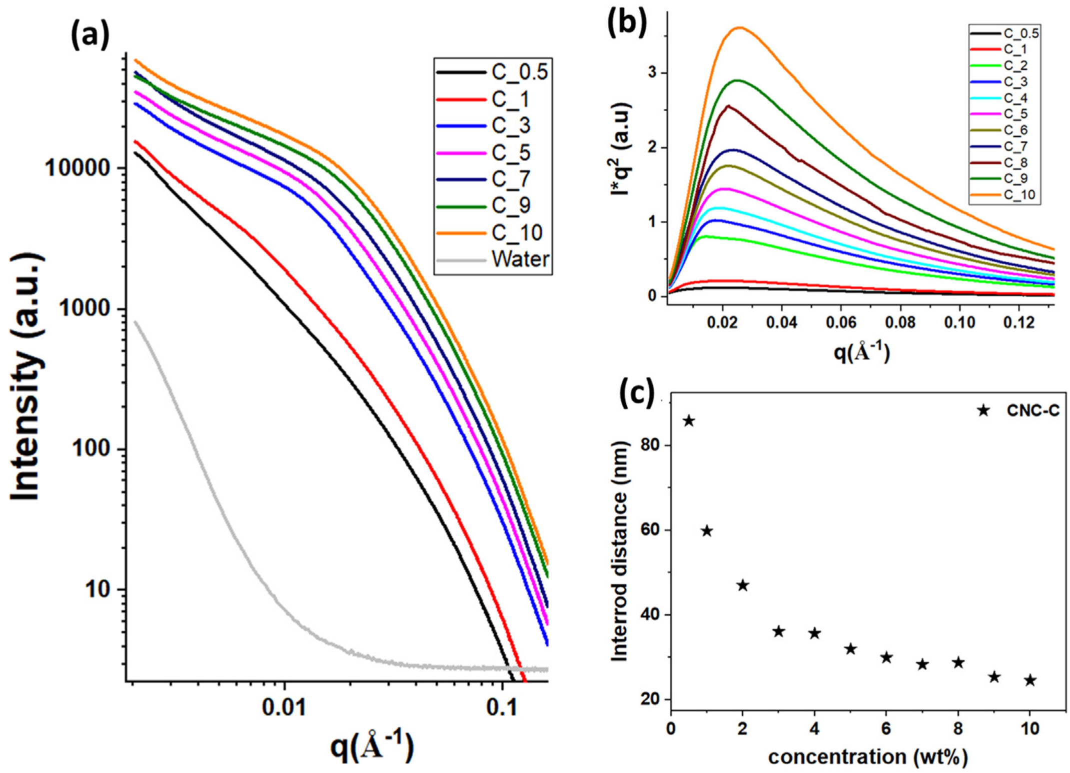

Fig. 5. (a) SAXS scattering curves of CNC-**C** of different concentrations ranging from 0.5 to 10 wt%. The grey curve is for the background from water. (b) The Kratky plot (I×q^2 vs q) of the SAXS curves given in (a). (c) The interparticle distance is plotted as a function of CNC-**C** concentration. The interparticle distance is extracted from the first peak position in the Kratky plot.

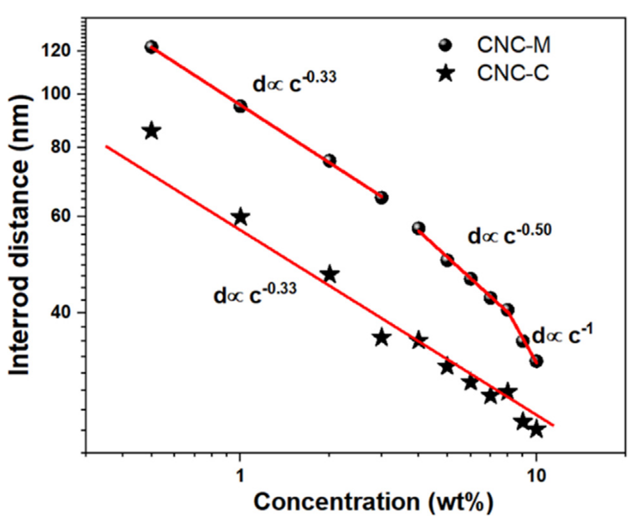

Fig. 6. Power law fitting of the interrod distance as a function of concentration. The CNC-**M** shows three different regions fitted with the $c^{-0.33}$, $c^{-0.5}$ and c^{-1}, while CNC-**C** only shows one fitted with $c^{-0.33}$.

where a, b, c are the edge lengths and $\Delta\eta$ is the scattering length density (contrast).

The lower wt% CNC suspension is used because the rods are non-interactive or poorly interactive, thus providing meaningful information on the distribution of size and shape. Fig. 7a shows the comparison of SAXS curves for 0.5 wt% CNC-**M** and CNC-**C**. The scattering curves are similar between q = 0.02–0.2 Å^{-1}. The scattering curve for q < 0.02 Å^{-1} shows two different slopes which are fitted with the power law $q^{-\alpha}$. The higher value of α = 1.8 is evaluated for CNC-**M** and there is a smaller value of α = 1.5 for CNC-**C**. For a non-interacting particle, a larger value of close to 2 reveals scattering from a disk, and a slope close to 1 indicates a rod shape. Moreover, the power law patterns with α value between 1 and 3 can also be interpreted as fractal aggregates [36]. The high value of α measured for CNC-**M** reveals either high width or diameter compared to the CNC-**C**, or they are poorly interacting and form fractal domains at lower concentrations [36]. This is in accordance with the large diameter distribution for CNC-**M** obtained from SAXS curve fitting (Fig. 7b). Furthermore, the interaction between the rod is extracted by evaluating the structure factor Sq(q) using the form factor F(q) of rectangular parallelepiped used for fitting by:

$$I(q) = F(q).S_q(q) \tag{4}$$

$$S_q(q) = \frac{I(q)}{F(q)} \tag{5}$$

The evaluated structure factor for CNC-**M** and CNC-**C** at different concentrations are shown in Fig. 7c. The Sq for the CNC-**M** at the lower concentration (1 wt%) showed a weak peak which reveals poor interrod interaction. The dominance in the peak increases with increasing rod concentration, and the peak position shifts towards higher q value. The dominance in the peak indicates increase in the interference between nearest neighbouring CNC-**M** rods with increasing concentration. The shift in the peak towards higher q values reveals a decrease in the interrod distance which is in consistent with the Kratky results analysis. The Sq intensity for the CNC-**C** are weak and the peaks are shallow which shows poor inter-rod interactions and weak interference between nearest rods.

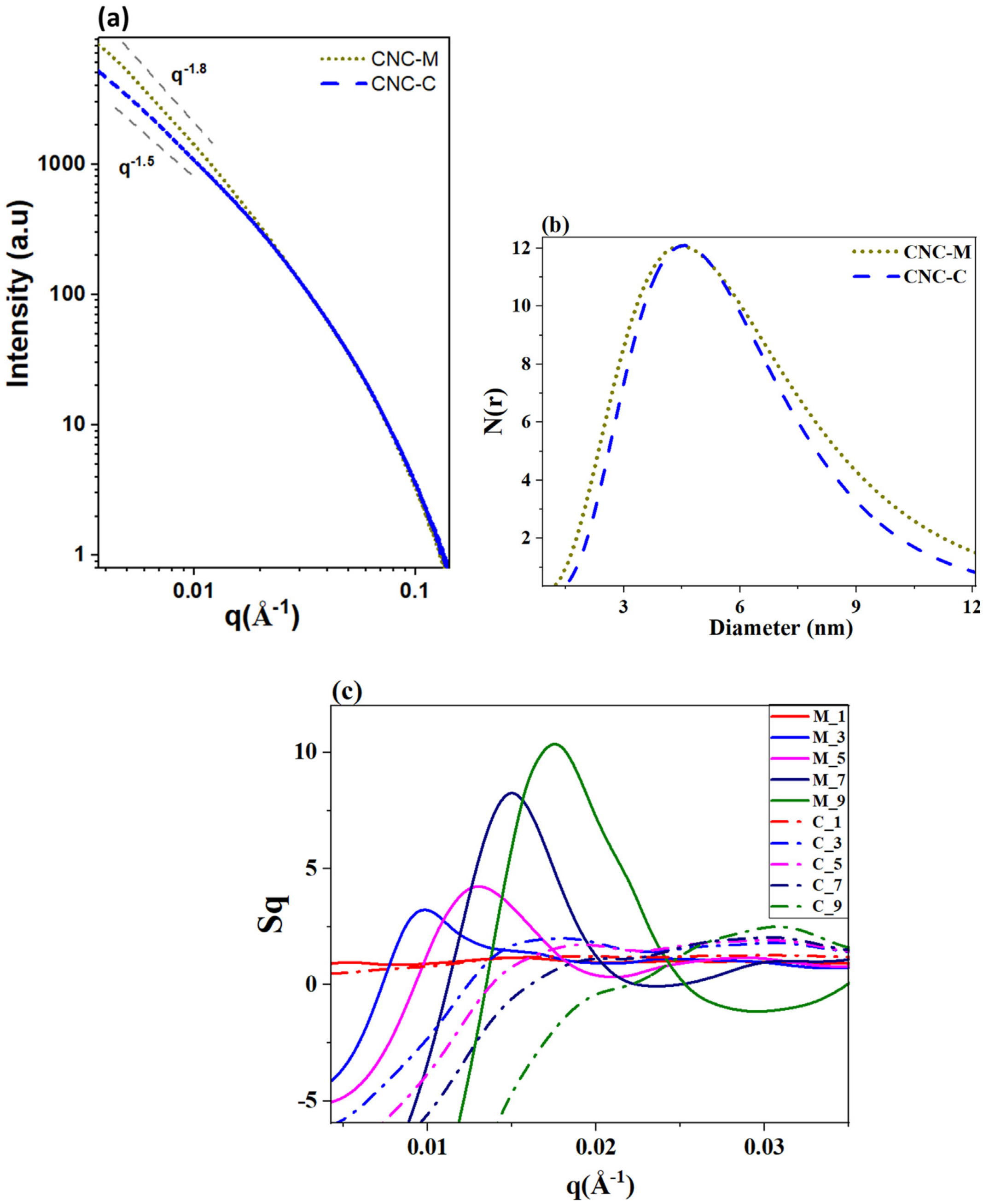

Fig. 7. (a) SAXS curves for the 0.5 wt% for CNC-**M** and CNC-**C**. (b) Fitting with the rectangular parallelepiped form factor reveals the log normal distribution of diameter. (c) The structure factor Sq evaluated by Eq. (5) for CNC-**M** and CNC-**C**.

4. DLVO modelling

The DLVO theory is used to calculate the potential energy between two different sets of rods aligned parallel and orthogonal (crossed) in a similar manner to Reid et al. [37]. The first set has a length of L = 80 nm and a diameter d = 5 nm, and for the second set, L = 160 nm and d = 5 nm. A surface potential of −50 mV at different ionic strengths ranging between 1 and 10 mM was used. The details of other parameters are provided in supporting information S2. The DLVO potential energy is calculated for both the cross and parallel alignment configuration of the rods (Fig. 8a). The resultant potential is calculated by taking the average of attractive and repulsive cross and parallel rods:

$$V = \frac{V_{cross} + V_{parallel}}{2} \quad (6)$$

With the crossed orientation of CNC, for both the 80 nm and 160 nm long rod sets (at a particular ionic strength), potential energy minima have the same magnitude and occur at a fixed separation distance (Fig. 8b, solid circle and open star). When the parallel arrangement of rods is considered the magnitude of potential energy minima value for the 160 nm rods being double of the 80 nm whilst the separation remains constant, which is primarily due to the area of interactions also being double (Fig. 8b, solid and open square).

CNC in suspension have several counter ions associated with the rods. When the CNC concentration is changed, as is the concentration of counter ions. The increase in CNC and counter ion con-

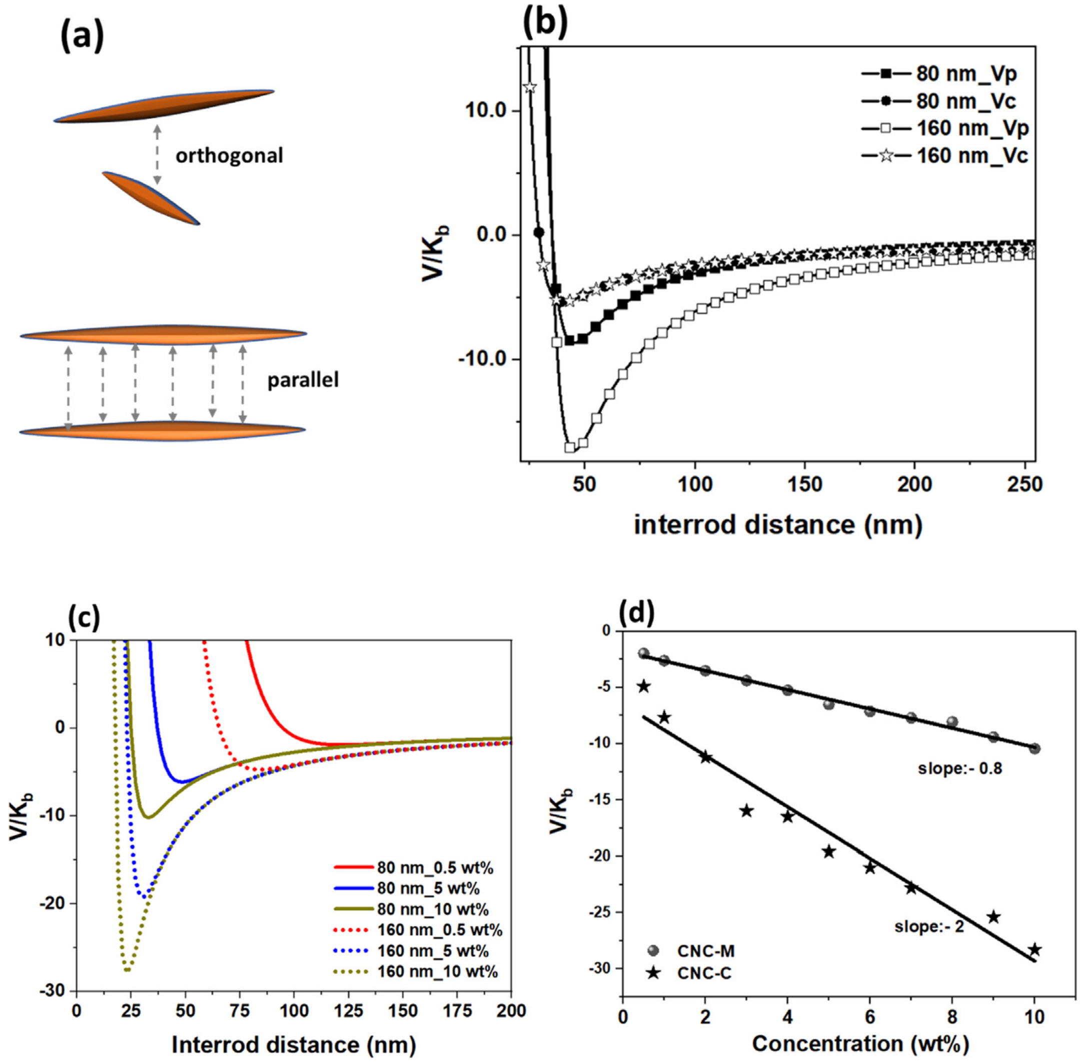

Fig 8. (a) Schematic of the parallel and orthogonal(cross) arrangement of rods. (b) Comparison of potential energy minima from DLVO for the cross (V_c) and parallel (V_p) aligned CNC rods of identical diameter 5 nm but different lengths 80 nm and 160 nm at ionic strength of 10 mM. (c) Averaged potential (parallel + cross)/2 calculated at different ionic strengths to calculate the interrod distance correlating with the concentration dependent interrod distance obtained from SAXS analysis. The potential energy minima for CNC 0.5 wt%, 5 wt% and 10 wt% were plotted (d) The evaluated potential from DLVO as a function of CNC concentrations. A linear fit was applied to evaluate the slope value.

centration leads to a reduction in interrod distance. DLVO calculations were completed with different salt concentrations to determine whether a potential energy minimum was present, indicating the crystals would be thermodynamically stable. The separation distance of this minima was compared to the interrod distance evaluated from SAXS. Table S3 in the supporting information shows the calculated interrod distance of the potential energy minima from DLVO for the two different lengths of 80 nm and 160 nm as a function of salt concentration. The salt concentrations are chosen in a way to match interrod distance calculated from SAXS for different CNC concentration.

Fig. 8c shows the change in the magnitude of the potential energy minima for both long (CNC-**C**) and short (CNC-**M)** rods at three different CNC concentrations (0.5 wt%, 5 wt% and 10 wt%) for different ionic strengths. Both long and short rods display an increase in the potential energy minima values as increases in the CNC concentration. However, the longer rods (CNC-C) have a higher potential energy minima value compared to the short rods. The interrod distance at these minima values decrease upon increasing ionic strength which is due to screening of the negative charges (decrease in EDL force). Fig. 8d shows the variation of the potential energy minima value as a function of CNC concentration. With an increase in CNC concentration the magnitude of the potential energy minima increases. The linear fit shows a higher slope (-2) for CNC-**C** compared to the CNC-**M** (-0.8). This indicates that the CNC-**C** have a dominating attractive force which leads to a higher potential energy minima magnitude due to being longer and having more associated counter ions than CNC-**M**.

For simplicity we have applied the DLVO approximation for interaction between monodispersed CNC rods of different lengths. However, in practice CNC rods are polydisperse and have a size distribution. To show the effect of CNC size distribution we have calculated the interaction potential energy of CNC rods of different size distribution at a fixed salt concentration of 10 mM and diameter of 5 nm. For shorter CNC-**M** rods, lengths from 60 to 100 nm with a mean length at 80 nm is used. For longer CNC-**C** rods lengths from 120 to 200 nm with a mean length at 160 nm is used. Changes in the magnitude of the potential energy minima for both long (CNC-**C**) and short (CNC-**M**) rods with different size distributions are provided in the supporting information (S4). The shaded region shows the assumed size distribution. Result indicates that at a fixed ionic strength the CNC size distribution only varies the magnitude of the potential energy minima without affecting the interrod distance.

5. Discussion

The self-assembly of two different types of commercial cellulose- CNC-**M** and CNC-**C** was compared at different concentrations ranging from 0.5 to 10 wt%. TEM micrograph showed the CNC-**M** rods are 88.9 ± 37.5 nm long and 5 nm in diameter. The CNC-**C** has nearly the same diameter (4–6 nm) as the CNC-**M**, but is twice as long (length 141.5 ± 60 nm). The diameter distribution determined from the SAXS curve fitting for both CNC rods at concentration of 0.5 wt% agrees with TEM results (Fig. 7b).

SAXS analysis reveals the short CNC-**M** rods self-assemble into different phases as concentration increases; an isotropic (0–4 wt %) to biphasic (4–7 wt%) to nematic (7–10 wt%) phase. Upon increasing concentration, the rods are organized in an ordered assembly of decreasing interrod distance from 122 nm to 33 nm. The anisotropy in the azimuthal averaging of SAXS scattering images shows self-assembly of CNC-**M** rods (supporting information S1). POM images agree with the SAXS results showing chiral nematic assembly of CNC-**M** rods. However, the long CNC-**C** rods have shown isotropic distribution throughout this concentration range with a decrease in interparticle distance (from 86 nm to 24.5 nm) upon increasing concentration. POM images for CNC-**C** show formation of randomly distributed tactoids which remain same at all concentrations. The isotropic azimuthal averaging of SAXS scattering images for CNC-C confirms and reveals the random distribution of CNC-C rods. (supporting information S1).

The self-assembly of CNC-**M** and CNC-**C** rods in different phases partially depends on the equilibrium between the attractive and repulsive forces. The attractive force is produced by the van der Waals (vDWs) interaction which depends on the dipole moments and interactions between molecules. The attractive force is responsible for bringing the rods closer. The counteractive electric double layer (EDL) force occurs due to the surface charges on the rods. The amount of charges on the CNC surface depends on the treatments applied to extract the CNC rods from the lignocellulosic source. The repulsive force brings deviation (orientation) from the parallel alignment of the CNC rods to introduce chirality [18]. The balance between attractive and repulsive force brings the rods to a finite interrod distance.

DLVO is a well-established theory to understand the balance between vDWs and EDL forces by plotting the potential energy as a function of interparticle distance. In this study, the DLVO calculation for the orthogonal (cross) arrangement for both long and short CNC rods have shown a similar separation and magnitude of the resultant potential minima (Fig. 8b). This is due to them having the same diameter and therefore the same interaction area. However, in a parallel alignment, the influence of van der Waals force starts at a larger distance for long rods and leads to lower potential energy minima which is due to the larger interacting area.

While increasing the CNC concentration, CNC-**C** experiences more surface charge screening due to higher counter ions concentrations (Fig. 8c). The vDWs force varies due to diameter, length of CNC, along with distance and Hamaker constant $A = 8.0 \times 10^{-21}$ J [38]. The longer CNC leads to a higher vDWs, but the apparent salt concentration is higher, leading to more screening of the EDL force. Thus, the dominating attractive interaction brings CNC-**C** closer (smaller interparticle distance) than the CNC-**M** (Fig. 5c). The dominating attractive force over the repulsive interaction for the longer rods does not allow rods to arrange in an ordered assembly. This leads to the formation of a gel network at lower CNC-**C** concentrations (gel point at 4.5 wt%) compared to the CNC-**M** sample (gel point at 8.5 wt%) [8,30]. Fewer rods come close and form smaller domains (Fig. 9). Furthermore, these domains are randomly oriented, as observed in the isotropic scattering images. The polarised optical microscopy and polarised optical photography reveals the similar results of isotropic and tactoid phases for the CNC-**C** sample [30]. The power law slope of $d = c^{-0.33}$ in Fig. 6 for CNC-**C** in the entire range reveals the isotropic distribution of rods and their domains [10]. Fig. 9 shows the schematic of the assembly of long rods at low, intermediate and higher concentrations.

In the smaller rods system of CNC-**M**, the DLVO calculation shows the attractive forces begin at a smaller distance and the resultant magnitude of the potential energy minima is nearly half compared to the long rods (Fig. 8b). At lower concentrations, the rods have poor interaction and thus they are randomly orientated in the suspension. This is justified by the slope of $d = c^{-0.33}$ (between 0.5 and 4 wt%) and the isotropic scattering image. Increasing concentration brings the rods closer where the rods start interacting with each other. The weak attractions bring the particles closer which is well compensated or balanced by the repulsive force which aligns rods in an ordered assembly. At intermediate concentrations (>4 wt%), both isotropic and nematic phase assemblies are present in the system. This is clearly observed by the slope of $d = c^{-0.5}$ (between 4 and 8 wt%) and the partial anisotropy in the scattering images. At the higher concentrations, the rods come much closer as observed by the decrease in the interrod distance. The balance between attractive and repulsive forces leads to aligned and self-assembled rods in a particular direction and increases ordering assembly. The slope change $d = c^{-1}$ (between 8 and 10 wt%) with anisotropic scattering confirms the presence of nematic ordered self-assembly [10]. Fig. 9 shows the schematic of the assembly of short rods at low, intermediate and higher concentrations.

Thus, the self-assembly of CNC is controlled by the magnitude of the repulsive and attractive interaction. When the attractive force is well compensated by the repulsive interaction, the rods have a high probability to align in a particular chiral nematic or nematic order. High magnitude of both attractive and repulsive interaction leads to aggregation or random distribution of rods. DLVO calculation proves that the long rods have dominating attractive force and thus need higher repulsive force compensation to arrange longer rods in chiral nematic and nematic order. CNC can be compared with other natural nanorods like tobacco mosaic virus (TMV) [39,40], filamentous bacteriophages (fd) [40] virus and Pf1 [41] which show isotropic, nematic or chiral nematic self-assembly in suspension. However, different factors relating to the surface charges, morphology [42], surrounding counterions and material composition and intrinsic properties balance the attractive and repulsive interaction forces and bring self-assembly. Besides extensive research on the organisation of nanorods in nematic and chiral nematic assembly, quantitative fundamental studies are still required to resolve unsolved mysteries of self-assembly mechanisms. This includes understanding the origin of chirality, and nematic and cholesteric phase at molecular and macroscopic level [40,42]. The current study contributes to a current and new understanding of how the length of CNC rods affects their assembly in suspension.

6. Conclusion

The self-assembly of cellulose nanocrystal (CNC-**M** and CNC-**C**) suspensions from two main commercial sources were studied by SAXS and POM. Concentrations ranging between 0.5 and 10 wt% were selected. Both CNC-**M** and CNC-**C** have a similar diameter ranging between 4 and 6 nm, but different length. TEM micrographs reveal the CNC to be rod shape and CNC-**M** to be shorter

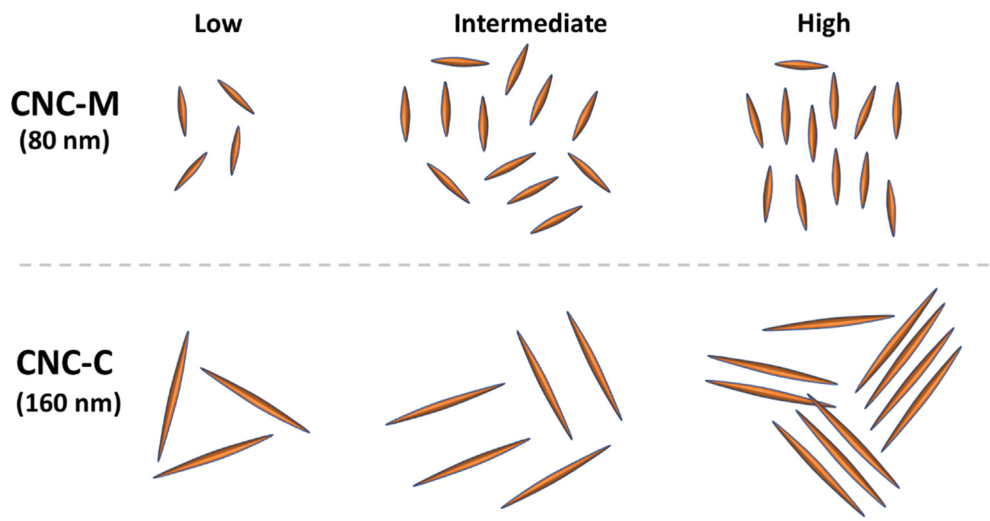

Fig. 9. (Top) Schematic of the self-assembly of CMC-**M** suspensions at different low isotropic (0–4 wt%), intermediate and (4–7 wt%) high concentration (>7 wt%). (Bottom) Self-assembly of the long CNC-**C** rods at different concentrations.

and more monodisperse in size than CNC-**C** [30]. The results are comparable with the CNC sizes of previous benchmarking of cellulose nanocrystals [29]. The diameter obtained from SAXS curves fitting agrees well with the TEM results. However, SAXS data analysis shows the CNC-**M** to be slightly thicker than the CNC-**C**.

Aqueous suspensions of the shorter CNC-**M** show an isotropic distribution of rods with a large inter-rod distance of 120 nm. Increasing CNC concentration decreases the interrod distance to 50 nm at 5 wt% with partial anisotropic distribution of the nematic assembly. At the higher concentration of 7 wt%, the rods arrange in a nematic assembly, showing an anisotropic distribution with an interrod distance of 32 nm. With increasing concentration, a large fraction of the CNC rods aligns in the nematic long-range order. The DLVO calculation suggests that for the smaller nanorods system, the weaker van der Waals (vDWs) attraction is well compensated by the repulsive force which helps align the rods in a particular direction. On the other hand, the long CNC-**C** rods isotropically distribute in suspension throughout the concentration range. The interrod distance is smaller compared to CNC-**M**. A decrease in interrod distance with increasing concentration is expected as the number of rods increases per unit volume. However, the long rods do not arrange in an ordered manner. DLVO calculations reveal the long rods have dominating vDWs attractive forces which overcome the repulsive interactions and hinders the long range self-assembly of nanorods. Thus, for the longer CNC rods with dominating attractive force required higher repulsive force to self-assemble with chiral nematic and nematic order.

The current study combines experimental SAXS and theoretical DLVO theory to improve the understanding on the interaction and self-assembly of colloidal CNC rods of different length in aqueous suspension. We demonstrated that depending on the morphology of CNC rods, a balance between attractive and repulsive interactions plays a crucial role in chiral nematic self-assembly. Previously, multiple studies were performed in understanding the self-assembly and aggregation kinetics of CNC rod of a particular length in aqueous suspension and solutions containing different salts [36,43,44]. Our work brings a new conceptual advancement in the mechanism in terms of colloid and interface science of self-assembly of nanoscale CNC rods of different length in a colloidal suspension regime which can be extended to the kinetically arrested regime [7].

Compensation of the dominating attractive interaction by higher repulsion in the long rod system can induce the self-assembly of the rods in a chiral nematic and nematic order. Thus, balancing the attractive and repulsive interaction in the commercial CNC by varying salt, pH, surface chemistry or through dialysis allows tuning the self-assembly of CNC rods into both the long- and short-range order [35,36]. Future work will focus on characterizing the SA of CNC rods at different pH, surface charges, and monovalent and divalent types of salts in a wide range of CNC concentrations. The fundamental knowledge to control the self-assembly of CNC of different morphology and surface composition enables the engineering of CNC functional composites for advanced technologies in optics, structure colours, electronics, batteries, biodiagnostics and sensor applications.

CRediT authorship contribution statement

Vikram Singh Raghuwanshi: Supervision, Investigation, Data curation, Methodology, Writing – original draft, Writing – review & editing. **Christine Browne:** Investigation, Data curation, Writing – review & editing. **Warren Batchelor:** Supervision, Writing – review & editing. **Gil Garnier:** Supervision, Writing – review & editing.

Data availability

Data will be made available on request.

Declaration of Competing Interest

The authors declare that they have no known competing financial interests or personal relationships that could have appeared to influence the work reported in this paper.

Acknowledgements

Financial support is from Australian Research Council (ARC), Australian Paper, Norske Skog, Orora, and Visy through the Industry Transformation Research Hub grant IH130100016. The authors thank Dr. Nigel Kirby beamline scientist of SAXS/WAXS beamline at the Australian Synchrotron for assistance during measurement, and the Australian Nuclear Science and Technology Organisation (ANSTO) for providing beamtime.

Appendix A. Supplementary material

Supplementary data to this article can be found online at https://doi.org/10.1016/j.jcis.2022.10.100.

References

[1] N. Grishkewich, N. Mohammed, J. Tang, K.C. Tam, Recent advances in the application of cellulose nanocrystals, Curr. Opin. Colloid Interface Sci. 29 (2017) 32–45.
[2] H. Zhu, W. Luo, P.N. Ciesielski, Z. Fang, J.Y. Zhu, G. Henriksson, M.E. Himmel, L. Hu, Wood-derived materials for green electronics, biological devices, and energy applications, Chem. Rev. 116 (16) (2016) 9305–9374.
[3] G. Delepierre, O.M. Vanderfleet, E. Niinivaara, B. Zakani, E.D. Cranston, Benchmarking cellulose nanocrystals Part II: New industrially produced materials, Langmuir 37 (28) (2021) 8393–8409.
[4] V.S. Raghuwanshi, S. Varanasi, W. Batchelor, G. Garnier, Cellulose nanocrystals to modulate the self-assembly of graphene oxide in suspension, Mater. Des. 216 (2022) 110572, https://doi.org/10.1016/j.matdes.2022.110572.
[5] R.M. Parker, T.H. Zhao, B. Frka-Petesic, S. Vignolini, Cellulose photonic pigments, Nat. Commun. 13 (1) (2022) 3378.
[6] M. Nasrollahzadeh, M. Sajjadi, S. Iravani, R.S. Varma, Starch, cellulose, pectin, gum, alginate, chitin and chitosan derived (nano)materials for sustainable water treatment: a review, Carbohyd. Polym. 251 (2021) 116986, https://doi.org/10.1016/j.carbpol.2020.116986.
[7] R.M. Parker, G. Guidetti, C.A. Williams, T. Zhao, A. Narkevicius, S. Vignolini, B. Frka-Petesic, The self-assembly of cellulose nanocrystals: hierarchical design of visual appearance, Adv. Mater. 30 (19) (2018) 1704477.
[8] C. Honorato-Rios, C. Lehr, C. Schutz, R. Sanctuary, M.A. Osipov, J. Baller, J.P.F. Lagerwall, Fractionation of cellulose nanocrystals: enhancing liquid crystal ordering without promoting gelation, Npg. Asia Mater. 10 (2018) 455–465.
[9] C. Honorato-Rios, J.P.F. Lagerwall, Interrogating helical nanorod self-assembly with fractionated cellulose nanocrystal suspensions, Commun. Mater. 1 (1) (2020), https://doi.org/10.1038/s43246-020-00069-z 69.
[10] Y. Liu, C. Schütz, G. Salazar-Alvarez, L. Bergström, Assembly, gelation, and helicoidal consolidation of nanocellulose dispersions, Langmuir 35 (10) (2019) 3600–3606.
[11] K.J. De France, K.G. Yager, T. Hoare, E.D. Cranston, Cooperative ordering and kinetics of cellulose nanocrystal alignment in a magnetic field, Langmuir 32 (30) (2016) 7564–7571.
[12] Y. Mao, M. Bleuel, Y. Lyu, X. Zhang, D. Henderson, H. Wang, R.M. Briber, Phase separation and stack alignment in aqueous cellulose nanocrystal suspension under weak magnetic field, Langmuir 34 (27) (2018) 8042–8051.
[13] Y. Habibi, T. Heim, R. Douillard, AC electric field-assisted assembly and alignment of cellulose nanocrystals, J. Polym. Sci., Part B: Polym. Phys. 46 (14) (2008) 1430–1436.
[14] T. Li, R.E. Winans, B. Lee, Superlattice of rodlike virus particles formed in aqueous solution through like-charge attraction, Langmuir 27 (17) (2011) 10929–10937.
[15] Y. Habibi, L.A. Lucia, O.J. Rojas, Cellulose nanocrystals: chemistry, self-assembly, and applications, Chem. Rev. 110 (6) (2010) 3479–3500.
[16] B. Thomas, M.C. Raj, K.B. Athira, M.H. Rubiyah, J. Joy, A. Moores, G.L. Drisko, C. Sanchez, Nanocellulose, a versatile green platform: from biosources to materials and their applications, Chem. Rev. 118 (24) (2018) 11575–11625.
[17] M.M. De Souza Lima, J.T. Wong, M. Paillet, R. Borsali, R. Pecora, Translational and rotational dynamics of rodlike cellulose whiskers, Langmuir 19 (1) (2003) 24–29.
[18] C. Schütz, M. Agthe, A.B. Fall, K. Gordeyeva, V. Guccini, M. Salajková, T.S. Plivelic, J.P.F. Lagerwall, G. Salazar-Alvarez, L. Bergström, Rod packing in chiral nematic cellulose nanocrystal dispersions studied by small-angle X-ray scattering and laser diffraction, Langmuir 31 (23) (2015) 6507–6513.
[19] S. Beck-Candanedo, M. Roman, D.G. Gray, Effect of reaction conditions on the properties and behavior of wood cellulose nanocrystal suspensions, Biomacromolecules 6 (2) (2005) 1048–1054.
[20] X.M. Dong, T. Kimura, J.-F. Revol, D.G. Gray, Effects of ionic strength on the isotropic−chiral nematic phase transition of suspensions of cellulose crystallites, Langmuir 12 (8) (1996) 2076–2082.
[21] L. Onsager, The effects of shape on the interaction of colloidal particles, Ann. Ny. Acad. Sci. 51 (4) (1949) 627–659.
[22] Z. Dogic, S. Fraden, Ordered phases of filamentous viruses, Curr. Opin. Colloid Interface Sci. 11 (1) (2006) 47–55.
[23] Y. Xu, A. Atrens, J.R. Stokes, A review of nanocrystalline cellulose suspensions: rheology, liquid crystal ordering and colloidal phase behaviour, Adv. Colloid Interface Sci. 275 (2020) 102076.
[24] M. Lin, V.S. Raghuwanshi, C. Browne, G.P. Simon, G. Garnier, Modulating transparency and colour of cellulose nanocrystal composite films by varying polymer molecular weight, J. Colloid Interf. Sci. 584 (2021) 216–224.
[25] S.L. Brenner, V.A. Parsegian, A physical method for deriving the electrostatic interaction between rod-like polyions at all mutual angles, Biophys. J. 14 (4) (1974) 327–334.
[26] A.A. Kornyshev, S. Leikin, Electrostatic interaction between long, rigid helical macromolecules at all interaxial angles, Phys. Rev. E 62 (2) (2000) 2576–2596.
[27] E.J.W. Verwey, Theory of the stability of lyophobic colloids, J. Phys. Colloid Chem. 51 (3) (1947) 631–636.
[28] B. Derjaguin, L. Landau, Theory of the stability of strongly charged lyophobic sols and of the adhesion of strongly charged particles in solutions of electrolytes, Prog. Surf. Sci. 43 (1–4) (1993) 30–59.
[29] M.S. Reid, M. Villalobos, E.D. Cranston, Benchmarking cellulose nanocrystals: from the laboratory to industrial production, Langmuir 33 (7) (2017) 1583–1598.
[30] C. Browne, V.S. Raghuwanshi, M. Lin, G. Garnier, W. Batchelor, Characterisation of cellulose nanocrystals by rheology and small angle X-ray scattering (SAXS), Colloids Surf., A 651 (2022) 129532, https://doi.org/10.1016/j.colsurfa.2022.129532.
[31] N.M. Kirby, S.T. Mudie, A.M. Hawley, D.J. Cookson, H.D.T. Mertens, N. Cowieson, V. Samardzic-Boban, A low-background-intensity focusing small-angle X-ray scattering undulator beamline, J. Appl. Crystallogr. 46 (6) (2013) 1670–1680.
[32] O. Glatter, O. Kratky, Small-angle X-ray Scattering, Academic Press, London, 1982.
[33] V.S. Raghuwanshi, U.M. Garusinghe, P. Raj, N. Kirby, A. Hoell, W. Batchelor, G. Garnier, Cationic polyacrylamide induced nanoparticles assembly in a cellulose nanofiber network, J. Colloid Interf. Sci. 529 (2018) 180–186.
[34] V.S. Raghuwanshi, A. Gallos, D.J. Mendoza, M. Lin, F. Allais, G. Garnier, Nanocrystallisation and self-assembly of biosourced ferulic acid derivative in polylactic acid elastomeric blends, J. Colloid Interf. Sci. 606 (2022) 1842–1851.
[35] M. Uhlig, A. Fall, S. Wellert, M. Lehmann, S. Prévost, L. Wågberg, R. von Klitzing, G. Nyström, Two-dimensional aggregation and semidilute ordering in cellulose nanocrystals, Langmuir 32 (2) (2016) 442–450.
[36] F. Cherhal, F. Cousin, I. Capron, Influence of charge density and ionic strength on the aggregation process of cellulose nanocrystals in aqueous suspension, as revealed by small-angle neutron scattering, Langmuir 31 (20) (2015) 5596–5602.
[37] M.S. Reid, S.A. Kedzior, M. Villalobos, E.D. Cranston, Effect of ionic strength and surface charge density on the kinetics of cellulose nanocrystal thin film swelling, Langmuir 33 (30) (2017) 7403–7411.
[38] L. Bergström, S. Stemme, T. Dahlfors, H. Arwin, L. Ödberg, Spectroscopic ellipsometry characterisation and estimation of the Hamaker constant of cellulose, Cellulose 6 (1) (1999) 1–13.
[39] F.C. Bawden, N.W. Pirie, J.D. Bernal, I. Fankuchen, Liquid crystalline substances from virus-infected plants, Nature 138 (3503) (1936) 1051–1052.
[40] E. Grelet, S. Fraden, What is the origin of chirality in the cholesteric phase of virus suspensions?, Phys Rev. Lett. 90 (19) (2003) 198302.
[41] Z. Dogic, S. Fraden, Cholesteric phase in virus suspensions, Langmuir 16 (20) (2000) 7820–7824.
[42] T.G. Parton, R.M. Parker, G.T. van de Kerkhof, A. Narkevicius, J.S. Haataja, B. Frka-Petesic, S. Vignolini, Chiral self-assembly of cellulose nanocrystals is driven by crystallite bundles, Nat. Commun. 13 (1) (2022) 2657.
[43] T. Cao, M. Elimelech, Colloidal stability of cellulose nanocrystals in aqueous solutions containing monovalent, divalent, and trivalent inorganic salts, J. Colloid Interf. Sci. 584 (2021) 456–463.
[44] H. Oguzlu, C. Danumah, Y. Boluk, Colloidal behavior of aqueous cellulose nanocrystal suspensions, Curr. Opin. Colloid Interf. Sci. 29 (2017) 46–56.